

LA-UR-18-29605

Approved for public release; distribution is unlimited.

Title: Primary Assessment Technologies FY2017 Milestone Report: NDSE Development Using DPF

Author(s): Olson, Russell Teall; Beller, Timothy Eugene; Boswell, Melissa; Cutler, Theresa Elizabeth; DeYoung, Anemarie; Dinwiddie, Derek Robert; Dugan, Timothy Michael; Fowler, Malcolm M.; Gomez, Jaime A.; Goorley, John Timothy; Harper, Arnold Kornahrens; Hayes-Sterbenz, Anna Catherine; Hayes, David Kirk; Hopson, John W. Jr.; Hutchinson, Jesson D.; Jungman, Gerard; Kamm, Ryan James; King, Robert S.; Koehler, Paul E.; Lash, Donald Keith; LeCounte, Ryan Dean; et al.

Intended for: Report

Issued: 2018-10-10

Disclaimer:

Los Alamos National Laboratory, an affirmative action/equal opportunity employer, is operated by the Los Alamos National Security, LLC for the National Nuclear Security Administration of the U.S. Department of Energy under contract DE-AC52-06NA25396. By approving this article, the publisher recognizes that the U.S. Government retains nonexclusive, royalty-free license to publish or reproduce the published form of this contribution, or to allow others to do so, for U.S. Government purposes. Los Alamos National Laboratory requests that the publisher identify this article as work performed under the auspices of the U.S. Department of Energy. Los Alamos National Laboratory strongly supports academic freedom and a researcher's right to publish; as an institution, however, the Laboratory does not endorse the viewpoint of a publication or guarantee its technical correctness.

Primary Assessment Technologies FY2017 Milestone Report: NDSE Development Using DPF

T. Beller, M. Boswell, T. Cutler, A. DeYoung, D. Dinwiddie, T. Dugan, M. Fowler, J. Gomez, S. Gonzales, J. Goorley, A. Harper, A. Hayes, D. Hayes, J. Hopson, J. Hutchinson, G. Jungman, R. Kamm, R. King, P. Koehler, D. Lash, R. LeCounte, J. Lestone, D. Lewis, H. Li, S. Lik, A. Lynn, J. Martin, G. McKenzie, T. McLaughlin, J. Miller, M. Mitchell, S. Mosby, G. Morgan, W. Myers, A. Obst, R. Olson, R. Rundberg, M. Snowball, L. Trujillo, K. Valdez, J. Walker, A. Wysong, V. Yuan

Los Alamos National Laboratory, Los Alamos, NM 87545

G. Arias-Tapar T. Austin, M. Axmann, R. Beaulieu, N. Bennett, P. Biancaniello, M. Blasco, J. Catenacci, D. Constantino, D. Dalley, V. DiPuccio, B. Foskett, J. Friedman, B. Gall, J. Gatling, C. Hagen², M. Heika, J. Irvin, R. Long, A. Luttmann, C. Manuel, T. Meehan, S. Merritt, S. Molnar¹, S. Owen, M. Powers, L. Robbins², J. Sargent, T. Sargent, N. Sipe, G. Skougard, J. Smith, R. Stueckrath, B. White

Nevada National Security Site, Mercury, NV 89023

1Powder River Geologic, LLC

2Keystone International, LLC

Summary:

A new diagnostic technique for a neutron-based measurement of dynamic subcritical experiments is currently under development. The technique, referred to as a Neutron Diagnosed Subcritical Experiment (NDSE), requires that a short intense burst of neutrons be directed into a subcritical fissile object and a precision measurement of the emitted fission gamma rays be made as a function of time. Recent advances in a dense plasma neutron source and gamma ray detectors have been integrated together at the Nevada National Security Site to provide a NDSE technique development and testing capability. The first set of NDSE demonstration experiments have now been completed using static objects constructed with large quantities of highly enriched uranium. The acquired data reveal the expected sensitivity to changes in neutronic properties of fissile objects and illustrate that the diagnostic approach is viable. As expected for any new measurement technique, many areas for improvement have been identified during static object testing and continued maturation of the diagnostic is planned before implementation on a dynamic subcritical experiment.

Introduction:

NDSE ultimately aims to measure the nuclear reactivity of weapons-relevant subcritical experiments thereby providing an integral constraint on the distribution and properties of the compressed special nuclear material (SNM). The measurement technique is analogous to reaction history measurements acquired during nuclear testing. In NDSE, multiple fission events are initiated in a subcritical

SNM object via a burst of externally generated neutrons. Unlike a nuclear test where the neutron population exponentially increased due to the positive reactivity of the device, the neutron population here rapidly decreases in the object at a rate that is directly related to the neutronic properties of the subcritical system itself. Prompt gamma rays are also produced at each fission event and are therefore proportional to the time-dependent neutron population. The “leakage” of these fission gamma rays from the SNM object is the NDSE observable quantity, but in the much more challenging regime of negative reactivity where ~ 10 orders of magnitude fewer fission gamma rays are emitted from the subcritical object than existed for supercritical devices.

Successful implementation of a NDSE measurement requires several key components: a short pulse neutron source; a fission gamma ray detector minimally affected by the fission and source neutrons; collimation and shielding to control background levels; and a fissile object that is slightly subcritical. Recent rapid developments in each of these areas have provided the ability to evaluate the viability of an NDSE measurement. Most notably, a short pulse dense plasma focus (DPF) neutron source has been developed at the Nevada National Security Site (NNSS), a Los Alamos National Laboratory LDRD-DR project developed a suitable set of gamma ray detectors, and both institutions designed and implemented a test stand at the NNSS Area 11 suitable for use with SNM static objects. The application of these technology developments to measurements with slightly subcritical SNM static objects and the resulting NDSE data are described here. The principal aim of these recent NDSE measurements was to demonstrate sensitivity of the technique to changes in the neutronic properties of SNM objects using the aforementioned technology advances.

SNM Static Objects:

The goal of the initial NDSE demonstration tests was to measure two SNM static objects that have different fission decay curves and thereby illustrate that the technique has sensitivity to this quantity. Suitable static objects had to satisfy several different requirements: 1) they must fall within the existing nuclear hazard categorization already established for the NNSS Area 11 Test Stand; 2) the SNM components must already exist with no additional SNM fabrication or modification required; and 3) the subcritical objects must be assembled by hand in the DAF and transported to Area 11 for testing. Meeting these requirements was essential because of resource and schedule constraints. Two suitable SNM static objects, Object #1 and Object #2, were designed based upon a review of the existing and available SNM components.

Object #1 uses polyethylene-reflected Rocky Flats Highly Enriched Uranium (HEU) shells 3-30. The assembled Rocky Flats hemispherical parts #3-30 has an air-filled interior and is enclosed inside two hemispherical aluminum shells that form a contamination barrier. This encased SNM object is surrounded by high density polyethylene (HDPE) hemispherical shells. Once encased in aluminum and the 6.3

cm thick HDPE shells, the outer diameter of the assembled object is 26.67cm with a total weight (21.726 kg HEU + 0.5059 kg Al + 8.39 kg HDPE) of approximately 30.6kg. The specifications of each component in the assembly are summarized in Table 1.

Table 1.

Material	Inner Radius (cm)	Outer Radius (cm)	Thickness (cm)	Density (g/cm ³)	Mass (kg)
Air	0.0	2.013	2.013	0.0012	-
Rocky Flats HEU Shells 3-30	2.013	6.671	4.658	18.530	21.726
Aluminum Shells AL30-1, AL30-2	6.67	6.972	0.328	2.670	0.506
HDPE shells 128Y1720642-5	6.985	13.335	6.300	0.960	8.39

The k_{eff} of the Object #1 was calculated for several scenarios with MCNP6 using the as-built model of Area 11. The model includes the various isotopes of uranium, but no alloying metals or trace elements. The computed k_{eff} of the bare HEU ball + Al shell is 0.74039 ± 0.00059 using the ENDF/B-VII.1 nuclear data set. The k_{eff} of the SNM assembly increases to 0.9501 ± 0.0006 when enclosed in the HDPE shells. Both the bare and HDPE reflected objects remain less than $k_{\text{eff}}=0.970$ even if completely surrounded by water or HDPE. If water completely filled the interior void and surrounds the test object, then the computed criticality increases to a “worst case” maximum $k_{\text{eff}} = 0.9764 \pm 0.00063$. The HDPE reflected ball has a k_{eff} of 0.955 ± 0.001 if it is sitting on the ground.

Object #2 uses polyethylene-reflected Rocky Flats Highly Enriched Uranium (HEU) shells 1-34. The assembled Rocky Flats hemispherical parts #1-34 are enclosed inside two hemispherical aluminum shells that form a contamination barrier. This encased SNM object is surrounded by high density polyethylene (HDPE) hemispherical shells. Once encased in aluminum and 2.0 cm thick HDPE shells, the outer diameter of the assembled object is 19.34 cm with a total weight (29.88 kg HEU + 0.5 kg Al + 1.80 kg HDPE) of approximately 32.2 kg. The specifications of each component in the assembly are summarized in Table 2.

The k_{eff} of the Object #2 was calculated for several scenarios with MCNP6 using the as-built model of Area 11. The model includes the various isotopes of uranium, but no alloying metals or trace elements. The MCNP6 model also contains both the stand and the inner convenience container (ICC) used to isolate the object from possible submersion in water. The computed k_{eff} of the bare HEU ball + Al shell is 0.840 ± 0.0004 using the ENDF/B-VII.1 nuclear data set. When enclosed in the HDPE shells, the k_{eff} of the SNM assembly increases to 0.9362 ± 0.0005 . When the HDPE reflected object is fully submerged in several meters of water without the ICC to isolate it, the “worst case” is a maximum of $k_{\text{eff}}=1.02$.

Table 2.

Material	Inner Radius (cm)	Outer Radius (cm)	Thickness (cm)	Density (g/cm ³)	Mass (kg)
Rocky Flats HEU Shells 1-34	0.00	7.334	7.334	18.534	29.88
Aluminum Shells 128Y1720643-3 128Y1720644-3	7.337	7.648	0.311	2.30	0.5042
HDPE Shells 128Y1720641-17 128Y1720642-17	7.676	9.675	2.019	0.943	1.8022

Because Objects #1 and #2 exceed 700 grams of ²³⁵U and require process-specific nuclear criticality safety controls due to hand assembly and disassembly, the operations must be conducted in nuclear hazard category 2 facilities. The current Area 11 hazard categorization doesn't meet these requirements so the solution is to assemble the test objects in the NNSS Device Assembly Facility (DAF), configure them in such a way that a criticality accident is precluded using only high-level or building-level nuclear criticality safety controls, and then transport them to the Area 11 Test Compound.

According to ANS-8.19¹, before a new operation with fissile material is begun or an existing operation is changed, it shall be determined and documented that the entire process will be subcritical for both normal and credible abnormal conditions. For the sake of efficiency, this task was broken down into the following three sub-tasks:

1. Criticality Safety Evaluation for Assembly, Active Interrogation, Radiation Measuring, Staging, Placement in a DPP-2 Type B Shipping Container, and Disassembly at the DAF.
2. CSI Determination for Transportation of the Target within a DPP-2 Type-B Shipping Container at the NNSS.
3. *Nature-Of-Process* Criticality Safety Evaluation for Handling, Active Interrogation, and Radiation Measuring at the Area 11 Test Compound.

According to ANS-8.1², the single-parameter subcritical-mass limit associated with ²³⁵U metal is 20,100 grams. This subcritical limit applies to a single piece of metal, which has no concave surfaces. This means that if one had a solid sphere of ²³⁵U

¹ ANSI/ANS-8.19, *Administrative Practices for Nuclear Criticality Safety*, 2014.

² ANSI/ANS-8.1, *Nuclear Criticality Safety in Operations with Fissionable Materials Outside of Reactors*, 2014.

metal having a mass that was no more than 20,100 grams and any reflection is bounded by thick water, subcriticality would be ensured.

Object #1 is comprised of ~20,345 grams of ^{235}U and is consists of 28 nesting hemi-shells all of which had concave surfaces. Therefore, additional criticality controls are necessary. Therefore, these shells are sealed within the aforementioned tight-fitting aluminum container before removal from the DAF as an additional high-level criticality safety control. Once inside this aluminum container, Object #1 remains subcritical with thick high-density polyethylene reflection and under all credible abnormal conditions.

Object #2 is comprised of ~27,845 grams of ^{235}U . This is ~38% higher than the reported subcritical limit and is constructed using 32 nesting hemi-shells all of which have concave surfaces. These shells are sealed within a tight-fitting aluminum container and held within the ICC of a DPP-2 shipping container using a centering fixture. Once inside the ICC, Object #2 remains subcritical with thick high-density polyethylene reflection and under all credible abnormal conditions.

For safety and security purposes, LANL certified fissile material handlers (FMHs) performed the assembly/material handling operations at the DAF and at the Area 11 Test Compound. Certified LANL personnel also performed the two-person custody duties for round-trip transportation of the static targets from the DAF to the Area 11 test compound and while the static targets resided at the Area 11 test compound during measurement campaigns.

DAF Measurements:

The main goal of the DAF experiments was the same as the ultimate NDSE static experiments goal; to measure the characteristic fission-chain decay of a sub-critical test objects, initiated by neutrons from an external source. Therefore, such measurements provide an independent, experimentally determined result that can be compared against SNM static object MCNP simulations and a measurement acquired at the Area 11 Test Stand. However, the DAF measurements were made over the course of many hours or days instead of in a dynamic single event, as is the ultimate NDSE goal. The advantages of the DAF measurements are that detailed data were acquired event by event in a relatively low-background environment and that the time characteristics of the neutron source do not appreciably affect the measured fission decay curve. Acquiring event-mode data allows more detailed tests of the same simulation code that will be used to interpret the ultimate NDSE experiments. For example, separate decay curves could be measured for γ rays and neutrons and detector pulse-height information could be used to reduce backgrounds as well as more cleanly diagnose differences between the simulations and the data.

Experimental Setup

At the DAF, the characteristic decay curve is determined by measuring fission γ rays as a function of time after the chain is initiated by an external neutron. This γ -ray die-off curve is constructed by measuring coincidence events between a detector registering the external neutron (the “start” signal) and another detector registering the emitted γ -ray (the “stop” signal). The system deployed was capable of discriminating between neutrons and γ -rays and so die-off (coincidence) curves could be measured for both. Because γ -rays all travel at the same speed whereas the neutron speed varies with energy, the measured γ -ray curve should more accurately reflect the actual die off of fission events in the system. Hence, the main emphasis is to validate the MCNP model of the γ -ray die-off curve. However, the neutron curve also provides additional useful tests of the simulations.

Data were taken using a CAEN DT5730, 14-bit desktop transient digitizer. The digitizer has 8 channels each capable of recording detector waveforms at 500,000 samples per second. Digital Pulse Processing-Pulse Shape Discrimination (DPP-PSD) firmware in the digitizer’s onboard field programmable gate array (FPGA) calculated output signals from the detector waveforms acquired together with precision timing information. Already widely used in various experiments at LANSCE, CAEN digitizers allow for asynchronous readout of the individual channels with near-zero dead time. Because the onboard 64-bit clock is common to all channels, time correlations between detectors can range from sub-nanosecond timescales to the order of many days. The digitizer was coupled to a Red Hat® 6 Linux machine built with an optical link PCIe card to maximize data transfer speeds to disk.

The CAEN software was modified to improve both speed and usability, allowing quick programming of desired settings such as trigger discrimination parameters, number of samples for each of the two charge integrals (detector pulse heights) along the waveform, and the length of the waveform to take once triggered. Each channel was self-triggered according to the programmed discriminator settings. Data from the digitizer were written to disk in the form of compressible binary files. A long-established routine (Replay Code) written to handle both compressed and uncompressed data from CAEN digitizers was used for quick replay of the data. To further guarantee the fidelity of the results, two additional independent replay codes were developed and it was verified that the results of the three codes were in agreement.

Prior to deployment, the data acquisition and replay system was tested in the Lujan Center at LANSCE using various configurations. A boron-loaded-polyethylene (B-poly) block, driven by an AmBe source was employed as a sub-critical-system surrogate. As neutrons emitted from the AmBe source moderated in the B-poly, some produced 478 keV γ -rays through the $^{10}\text{B}(n,\alpha\gamma)$ reaction. This γ -ray signal dies

off in a fashion similar to the fission-chain die off from a neutron-driven sub-critical system. The advantage of the B-poly is that it can be used without criticality rules and regulations.

The system was tested with lanthanum bromide (LaBr), bismuth germinate (BGO), and liquid-scintillator detectors. A picture of the test setup with two LaBr detectors is shown in Fig. 1. Detection (in the LaBr or BGO detectors) of a 4.44 MeV γ -ray from the AmBe source served as the start signal indicating a neutron had been emitted by the source. Detection (in the LaBr or liquid scintillator detectors) of the 478 keV γ -ray from the $^{10}\text{B}(n,\alpha\gamma)$ reaction served as the stop signal. Gates were set around the regions of these γ -rays in the pulse-height spectra during replay to improve signal-to-noise ratio. In addition, the long- and short-time integrals output by the DPP-PSD firmware were used with the liquid-scintillator detectors to calculate pulse shape and thus separate detected γ -rays from neutrons. Excellent separation of γ -rays and neutrons was demonstrated as shown in Fig. 2.

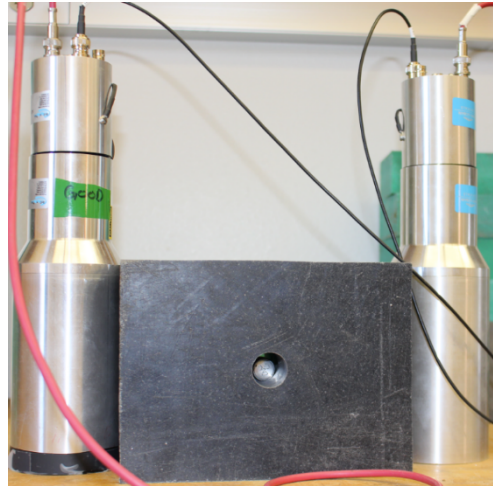


Figure 1. Picture of one configuration of the B-poly-block (black rectangular object with hole) test setup using two LaBr detectors. The AmBe neutron source can be seen inside the hole in the B-poly block.

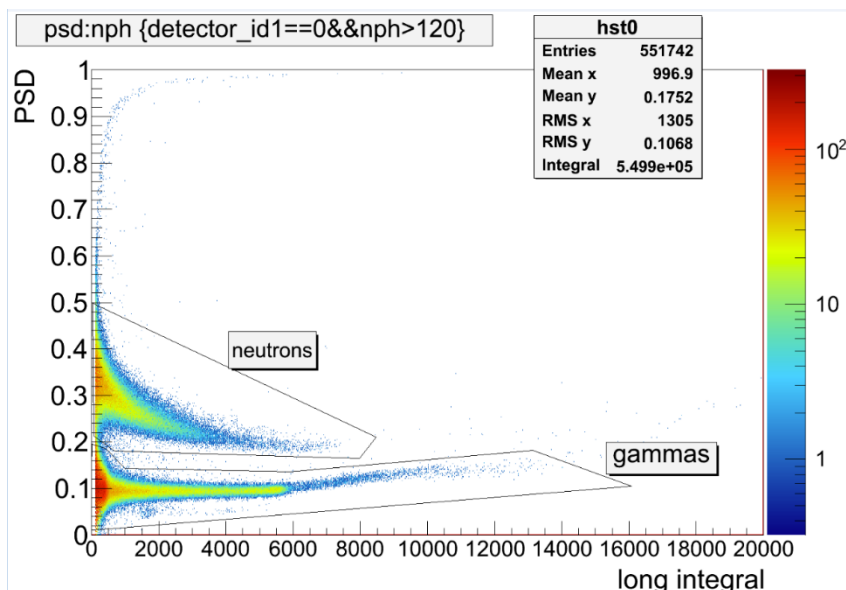


Figure 2. Example pulse-shape-discrimination (PSD) spectrum. The short and long integrals from the DPP-PSD software were used to calculate the $PSD = (long - short)/long$.

MCNP was used to calculate the expected γ -ray die-off signal. The slope of the die off was calculated to depend on the relative boron content and density of the B-poly block and, to a lesser extent, on the size and shape of the block. Excellent agreement between the measurements and calculations was found for all detector combinations and configurations (source inside or outside the block) run. Fig.3 shows an example the good agreement obtained. Successful completion of these tests indicated the system was capable of the planned HEU experiments at the DAF.

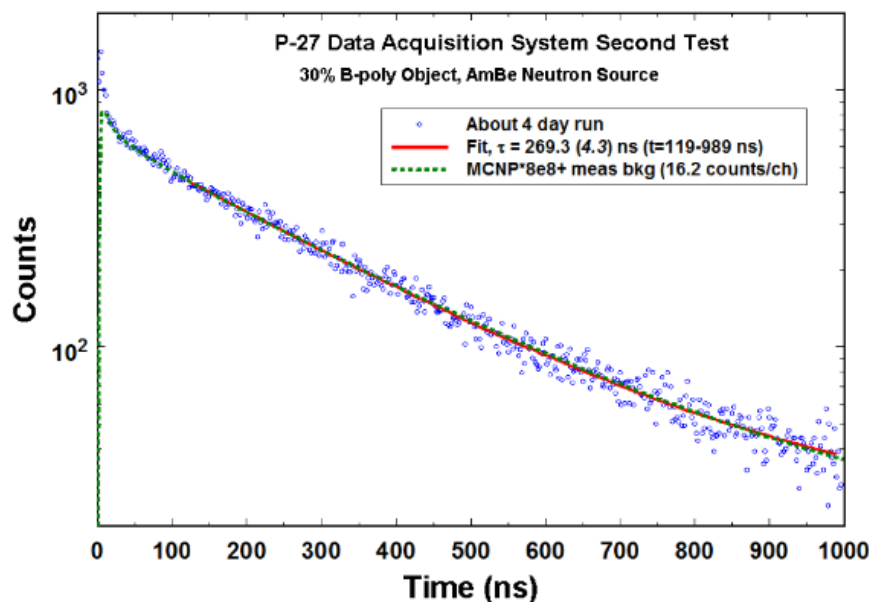


Figure 3. Example good agreement between measurement of the γ die-off from an AmBe-driven B-poly block and MCNP simulations.

A schematic diagram and photograph of the DAF setups are shown in Fig. 4. A low-mass stand comprised of aluminum plates and cylinders and steel rods was

designed to reduce room-return background by elevating the source, object, and detectors from the floor. Fig. 4 illustrates how the spherical Object #1 was held in place by two aluminum cylinders. It also shows that the cylindrical ICC enclosing Object #2 was held in a similar fashion. The circular plate below the object served to hold the external neutron source and detectors. The source and detectors can be seen to the left and right, respectively, of Object #2 in Fig. 4. The source was placed on a scissor jack to allow it to be vertically aligned with the center of the object. The detectors were held in a stand made from 80/20 aluminum pieces. The 180-degree configuration, in which the source, object center, and center of the detectors are aligned along a common axis, is shown for Object #2 in Fig. 4. For the 90-degree configuration, the detectors were rotated about a vertical axis passing through the center of the object by 90 degrees from the location shown in Fig. 4.

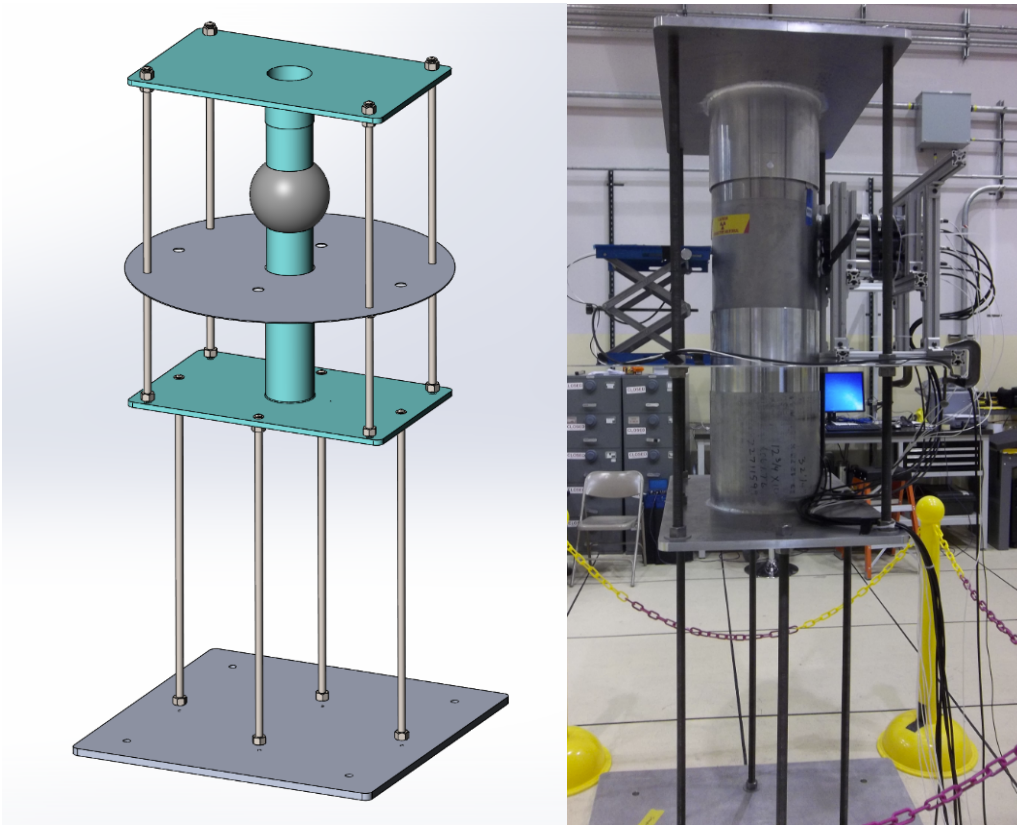


Figure 4. Schematic diagram of the stand used for the DAF experiments holding Object #1 (left). Picture of the DAF setup used for Object #2 (right). See text for details.

Object #1 Measurement and Results

Two different external neutron sources were used to initiate fission chains in Object #1; ^{252}Cf and AmBe . A bismuth germanate (BGO) scintillator detector was used to generate start signals for the coincidence data-replay system by detecting γ -rays emitted at the same time as neutrons from the external source. Six liquid-scintillator detectors were used to detect (and differentiate) fission γ -rays and neutrons

produced by Object #1, thus supplying stop signals for the coincidence replay of the data. The ^{252}Cf source had the advantages that it was more intense, resulting in better statistical precision compared to AmBe, and that ^{252}Cf spontaneous fission events produce several γ -rays, thus ensuring nearly 100% efficiency for tagging source neutrons. Unfortunately, these ^{252}Cf spontaneous-fission γ -rays could not be distinguished from fission γ -rays originating in Object #1 itself. This resulted in a fairly large background in the coincidence spectrum at short times that had to be subtracted. The AmBe source had the advantage that a very clean tag for when a source neutron was emitted could be generated by detecting 4.44 MeV coincidence γ -rays from the $^9\text{Be}(\alpha, n)^{12}\text{C}^*(\gamma)$ reaction. Unfortunately, only about 10% of the emitted neutrons emitted by the AmBe source result from this reaction, so there were many untagged neutrons entering Object #1 with this source. Also, the detection efficiency for this 4.44-MeV γ -ray was less than 100%, resulting in larger ambient background with this source.

Three geometry/source configurations were run with Object #1. The ^{252}Cf source was placed on the opposite side of Object #1 from the six liquid scintillator detectors (180-degree configuration). The AmBe source was run at both 90 and 180 degrees. The 180-degree configuration better shielded the liquid-scintillator detectors from direct source γ -rays and neutrons, but most of the γ -rays and neutrons detected from Object #1 in this configuration originated from the hemisphere closest to the detectors (because Object #1 itself acts as a strong attenuator). The 90-degree configuration resulted in better sampling of fission events from the front (nearest the external source) and back hemispheres of Object #1, but had higher background from the external source.

Backgrounds were subtracted by reflecting the negative-time (BGO signal detected after a liquid-scintillator signal) data. As shown in Fig. 5, this resulted in good agreement for the γ die-off coincidence spectra measured in all three configurations for times greater than about 30 ns. The AmBe data in this figure at 90 and 180 degrees were normalized (due to different run times and source strength) by factors of 37 and 24, respectively. Spectra of similar quality also were obtained for the die off of the neutron signal.

These same data also were replayed using the well-known Rossi- α and Feynman-variance-to-mean techniques. These data appear to be useful for benchmarking purposes. Although comparisons are still ongoing and beyond the scope of this report, there appears to be good agreement between the three replay techniques.

Object #1 data also were taken with bare and moderated ^3He neutron detectors using three different (^{252}Cf , AmBe, and a pulsed 14-MeV neutron source) external neutron sources. These measurement systems are sensitive to fission-chain decay time constants on the order of 100 μs and so the results can be compared to the longest time constant measured by the liquid-scintillator-based (LS) system described above. The ^3He -detector data were replayed using the Rossi- α and

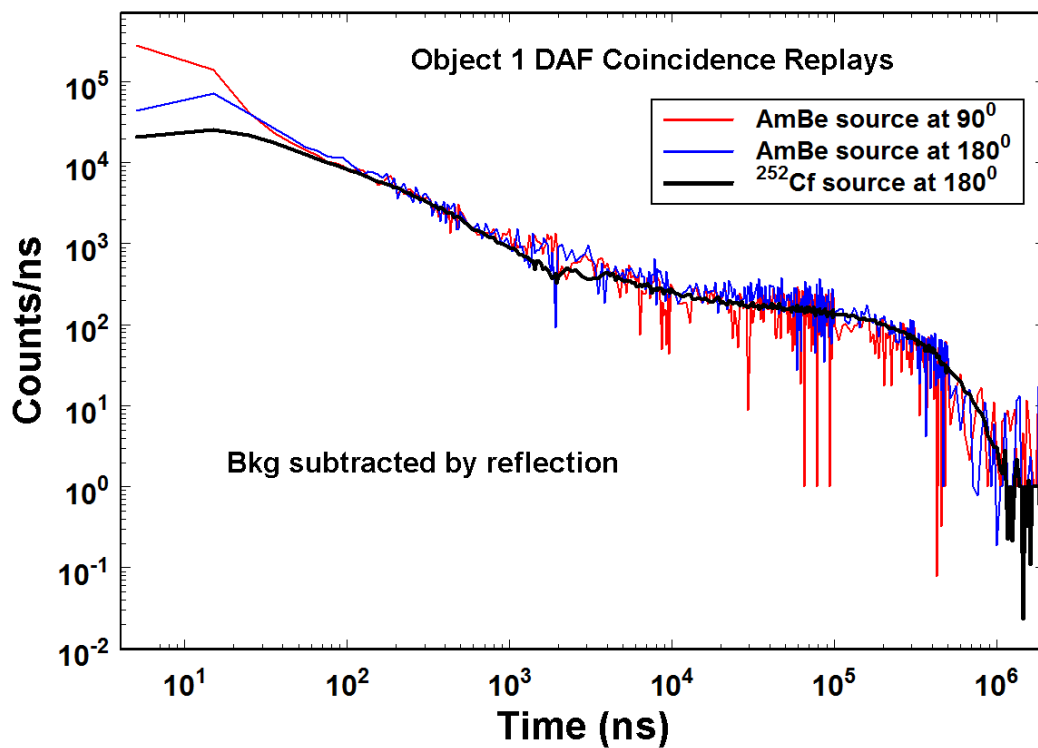


Figure 5. Coincidence spectra for Object #1 at the DAF measured with three different configurations. See text for details.

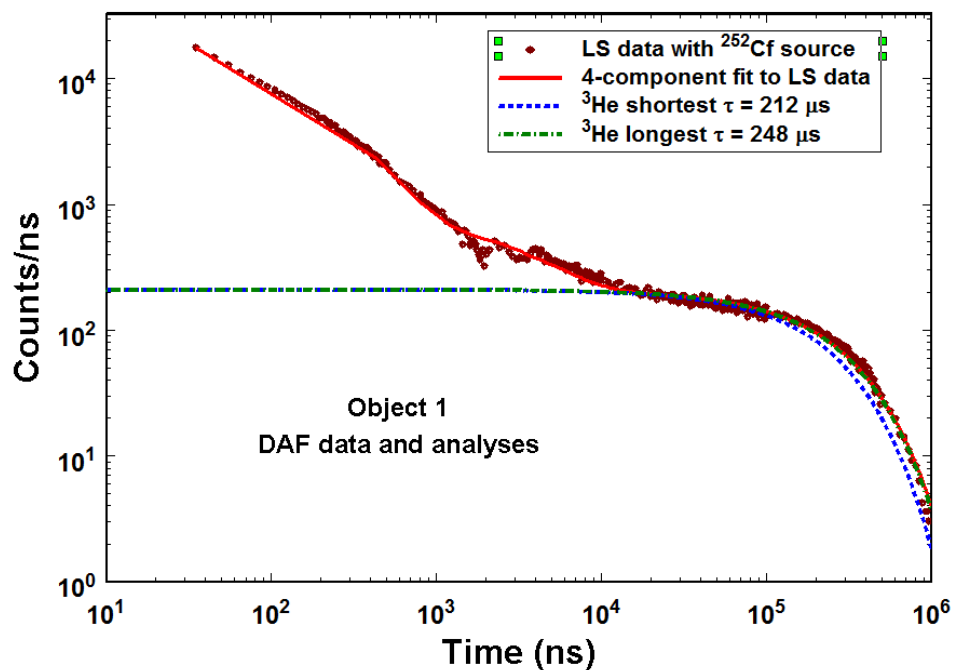


Figure 6. Comparison of LS data for object 1, a four-component exponential fit to these data, and the shortest and longest time constants determined by ^3He -detector data for Object #1.

Feynman-variance-to-mean methods and a single time constant τ was extracted for each case by fitting the data to an exponential function; $Counts = Ae^{-t/\tau}$, where A is a normalization constant. The setup employing moderated ^3He neutron detectors necessitated inclusion of a second time constant in the fitting procedure to account for the moderation time of the detector. Fitted time constants ranged from 212 ± 8.2 to 241.7 ± 0.7 μs , where the uncertainties are one-standard-deviation statistical uncertainties. A reasonable description of the LS data required at least four exponential components, all due to Object #1 itself; $Counts = Ae^{-t/\tau_1} + Be^{-t/\tau_2} + Ce^{-t/\tau_3} + De^{-t/\tau_4}$. The longest time constant from the fit to the LS data, $\tau_4 = 253 \pm 26$ μs , is consistent with the ^3He -detector results. A graphical comparison of the LS and ^3He -detector results, as well as a four-component exponential fit to the LS data is shown in Fig. 6.

Object 2 Measurement and Results

The data acquisition and replay systems for Object #2 were the same as for Object #1 with one important improvement; the external source was ^{252}Cf inside a fission chamber. This change resulted in a much cleaner start signal for coincidence replay and hence much lower background at short times. As a result, only a constant (in time) background needed to be subtracted from the data, and this could be determined with extremely high precision using the data at negative times.

Measurements were made with relatively weak (8.9×10^2 fissions/s) and stronger (1.68×10^4 fissions/s) ^{252}Cf sources. Comparison of results obtained with these two sources provided a check of the background subtraction. As shown in Fig. 7, there is excellent agreement between the two sets of data over five orders of magnitude in dynamic range.

There also is excellent agreement between Object #2 coincidence data taken with the 90- and 180-degree configurations, as shown in Fig. 8. As expected, the 90-degree data are larger at short times because the liquid-scintillator detectors see a larger number of γ -rays and neutrons directly from the ^{252}Cf source in this configuration compared to the 180-degree one (where Object #2 more effectively shields the liquid-scintillator detectors from the ^{252}Cf source). The short-time difference should be a further good test of MCNP's simulation capabilities.

The measured γ die off from object 1 is compared to Object #2 in Fig. 9. As expected, the slopes of the die-off curves are very different for the two objects, due to their different ratios of HEU to polyethylene. These are exactly the desired neutronic characteristics needed for a static NDSE feasibility demonstration at the Area 11 Test Stand.

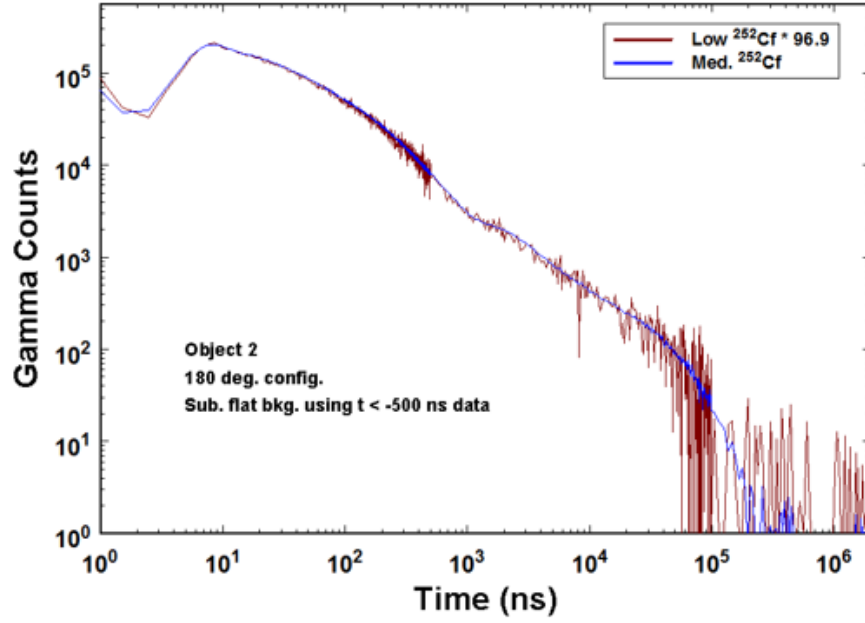


Figure 7. Comparison of Object #2 γ die off curves measured with the low- and medium-rate ^{252}Cf sources. There is excellent agreement between the two sets of data across five orders of magnitude in counts and time.

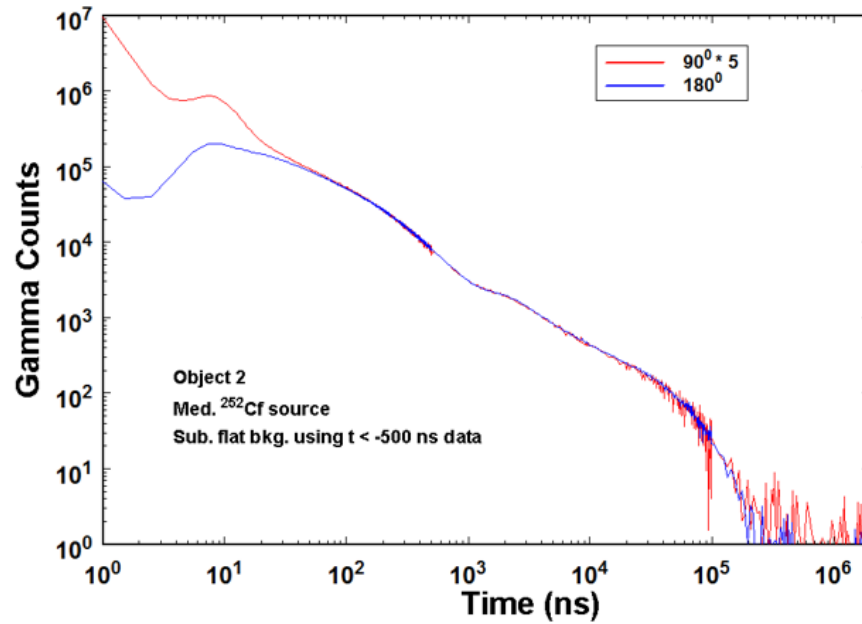


Figure 8. Comparison of Object #2 coincidence replay results for the 90- and 180- degree configurations. After the expected difference at short time, there is excellent agreement between the two sets of data.

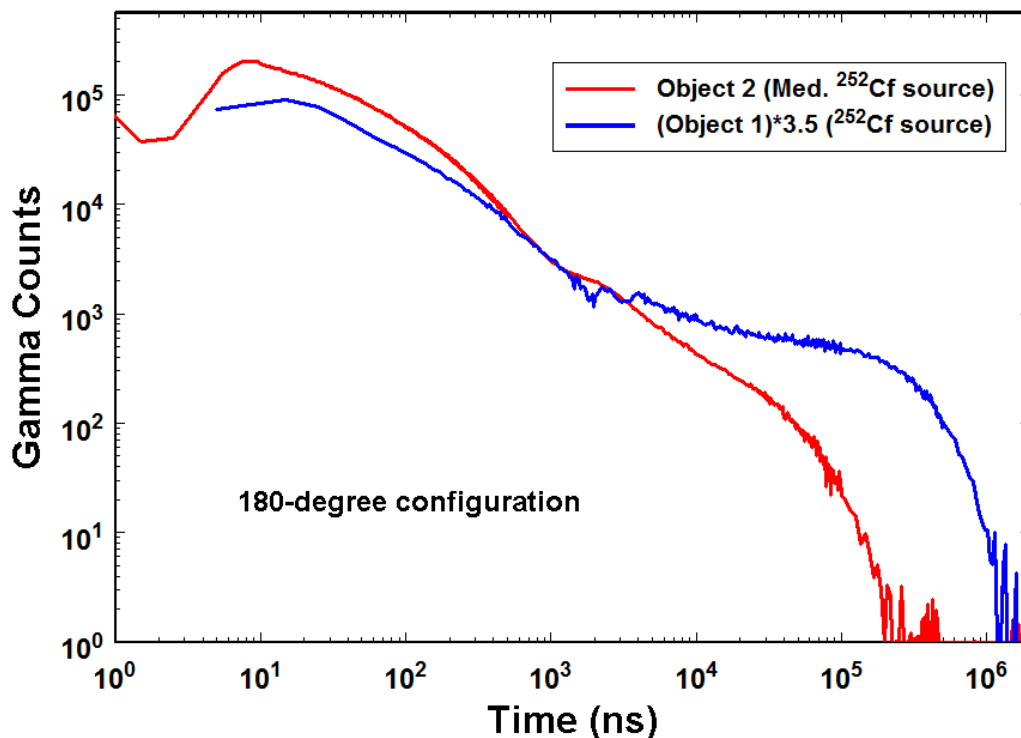


Figure 9. Comparison of measured γ -die-off curves for Objects #1 and #2.

As shown in Fig. 10, clean discrimination between γ -rays from neutrons was achieved and so separate neutron die-off curves were obtained for both Objects #1 and #2. As an example, the γ -ray and neutron die-off curves for Object #2 for the 180-degree configuration are compared in Fig. 10. Because neutrons travel more slowly than γ -rays, the peak of the neutron curve is delayed compared to the γ -ray curve. Also, the shape of the neutron energy spectrum is expected to shift towards lower energies at later times and the detection efficiency varies considerably with energy. Therefore, as can be seen in Fig. 10, the slopes of the γ -ray and neutron curves differ, providing additional tests of the simulation capabilities of MCNP.

A final DAF measurement was made with a bare Object #2 (without its surrounding polyethylene shell). This resulted in a much shorter time constant for the system as shown in Fig. 11 and thus provides yet another test of the simulation capabilities of MCNP.

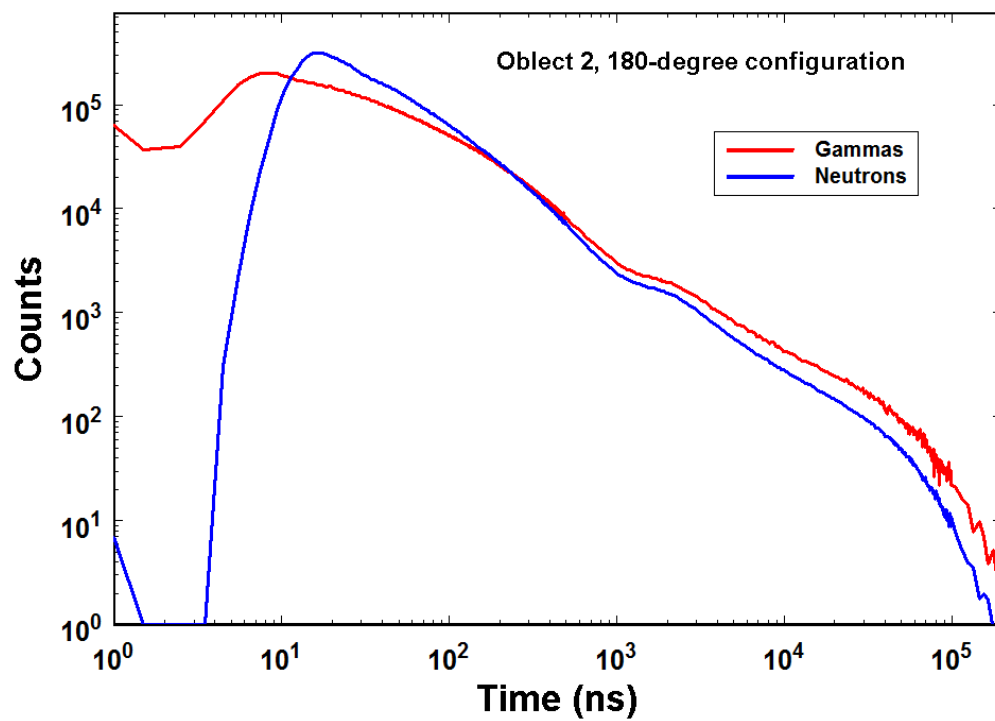


Figure 10. Neutron and γ -ray die-off curves for Object #2.

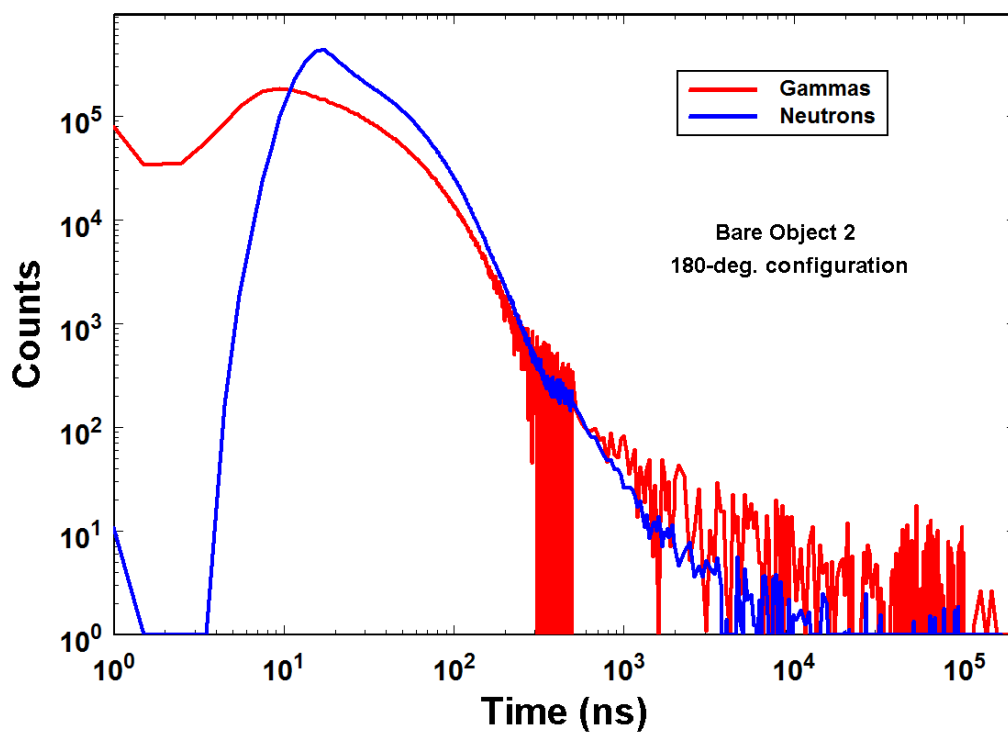


Figure 11. Neutron and γ -ray die-off curves for Object #2 measured without its surrounding polyethylene shell.

With essentially three different objects (Object #1, Object #2 “dressed”, and Object #2 “bare”), two different configurations (90 and 180 degrees) per object, and separate γ -ray and neutron die-off curves, the DAF measurements represent 12 separate data sets for validating the MCNP models. In addition, the detector pulse height (γ -ray or neutron energy) and detector number (for each of the six liquid-scintillators) were recorded for each event. These parameters can be used during replay to further test and improve the MCNP simulations. For example, preliminary replay data for Object #2, separating the data at different die-off times by γ -ray energy, indicates that data at short times (≈ 10 ns) show the presence of appreciable inelastic γ -rays from iron. This suggests it will be important to include nearby support material in the MCNP model in addition to the source, object, and detectors.

Area 11 Test Stand Measurements:

Prior to FY17, there had been no DPF campaign at Area 11 that involved the use of Special Nuclear Materials, so there were significant administrative and regulatory controls that had to be put in place to accommodate the higher-hazard experiments. Administrative controls were added to the Area 11 operations procedures that ensured that no personnel entered the compound in the presence of the target, except when escorted by appropriate security personnel and trained material handlers. All team members were also required to enter and exit through a security checkpoint, ensuring that no material was inappropriately removed from the compound. A new security fence was installed around the facility, providing a secondary barrier to facility access. The Centerra Nevada security force was engaged to carry out a vulnerability analysis, which resulted in an Incident Response Plan for the facility, and a force-on-force exercise was performed to ensure that the plan was sufficient for the facility. Completion of these facility upgrades enabled pulsed mode NDSE measurements of the fission decay curve of Objects #1 and #2 that could be compared against those obtained at the DAF.

Area 11 Experiment Setup: Neutron Source

While there are several possible approaches to initiating the requisite number of fission events for an NDSE measurement, a dense plasma focus (DPF) is one of the most promising technologies. A DPF is a device consisting of two coaxially located electrodes with a high-voltage source at one end. In the presence of a low-pressure gas, the high-voltage source induces an electrical breakdown across an insulator and the formation of a current-conducting plasma sheath at the upstream end of the DPF. During the so-called “run-down” phase, the current sheath is accelerated down the length of the electrodes by magnetic pressure, ionizing and sweeping up neutral gas as it accelerates. When the plasma sheath (involved in the run-in) reaches the end of the inner electrode, a portion is pushed radially inward during the so-called “run-in” phase. When the leading edge of the current sheath reaches the central axis, under the strong azimuthal magnetic pinch force, the plasma creates a hot, dense region (called a “pinch”) that emits high-energy electron and ion beams, x-rays, and (in the presence of deuterium or deuterium-tritium gas) fusion neutrons.

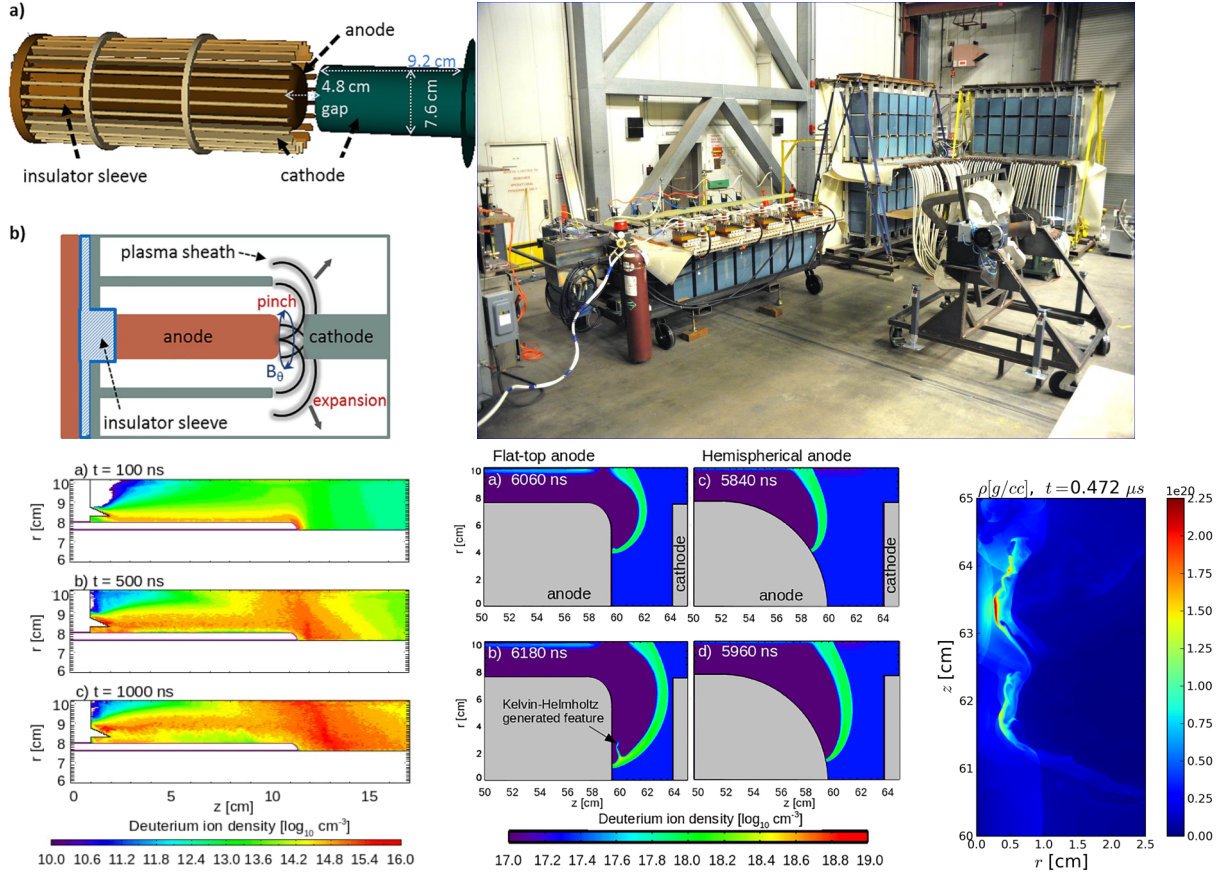


Figure 12. Schematic of the Dense Plasma Focus head, above left, along with the Area 11 capacitor bank, above right, used for the first SNM static demonstration experiments; on the bottom are simulations from the *Chicago* and LA-COMPASS codes predicting the insulator breakdown processes, the influence of anode design on electrical performance, and the detailed plasma instabilities leading to DT pinches.

The DPF concept was invented and developed in the late 1950's by Colgate, Filippov and Mather. However in the last few years, NNSS successfully developed a deuterium-tritium (DT) DPF (see Fig. 12) with a 350 kJ stored-energy capacitor bank and a new reentrant cathode design where only a small A-K gap exists in the “pinch” region. This new DPF geometry reduces the typical neutron pulse length by suppressing the formation of multiple pinches. Initially these advances were discovered through empirical experimentation, but recent simulation efforts by NNSS, LANL, and Voss Scientific have improved physics understanding of the reentrant DPF performance. Simulations using the LA-COMPASS MHD-code and the *Chicago*-hybrid PIC code can now predict the initial insulator electrical breakdown and ionization of the DT gas, electrical performance of the DPF as a function of anode design, and the detailed pinch physics process created by magneto-hydrodynamic plasma instabilities.

A dynamic, subcritical nuclear reactivity measurement requires a short-duration, high-yield neutron pulse with precise timing. The duration of the pulse is measured by the full-width at half max (FWHM), full-width at tenth max (FWTM), and the fall time (time duration for the pulse to decay from 90% of the peak height down to

10% of the peak height) of the signal measured by a neutron detector installed near the DPF tube. Figure 13 illustrates these pulse metrics, as calculated from a measured signal from the so-called “near-in” neutron detector at the Area 11 DPF. A “good” neutron pulse is one where the yield is greater than 10^{12} neutrons, and the FWHM, FWTM, and fall time are less than 75, 200, and 75 ns, respectively. However, a pulse may be “adequate” for a dynamic reactivity measurement even if not all the “good” metrics are met. This determination is achieved through detailed simulation studies where the pulse profiles are input into a MCNP model of a dynamic experiment.

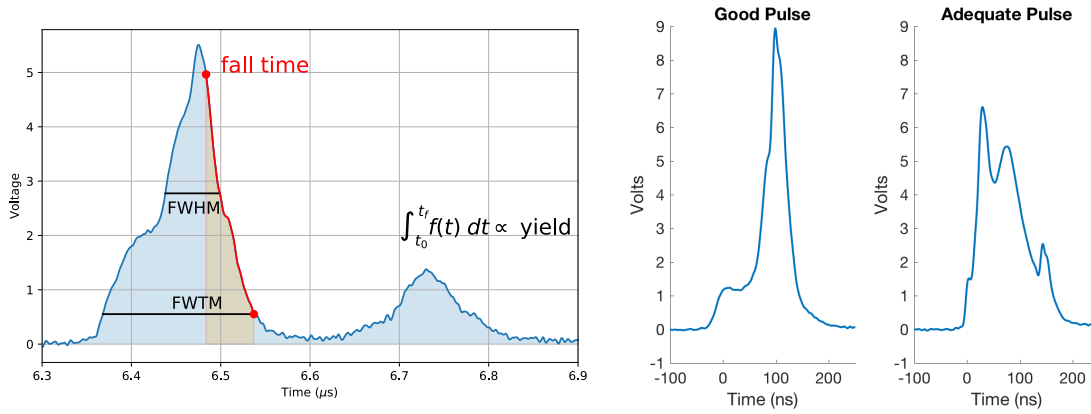


Figure 13: Example of the metrics used to characterize the DPF neutron pulses is shown on the left. The FWHM, FWTM, and fall time are labeled on the pulse, and the shaded region under the curve (blue + beige) is proportional to the total yield. Examples of “good” and “adequate” pulses are shown on the right. The “good” pulse has a FWHM of 41.8 ns, FWTM of 155.3 ns, a 90%-10% fall time of 38.8 ns, and a yield of 1.23×10^{12} neutrons. In comparison, the “adequate” shot on the right has a FWHM of 86.5 ns, FWTM of 174.0 ns, a fall time of 84.8 ns, and the shot had a yield of 1.71×10^{12} neutrons.

There were 42 DT shots produced by the NNSS DPF over a 8 day period during the acquisition of Object #1 fission decay curve measurements. All 42 neutron pulses were evaluated through subsequent MCNP simulations to be “adequate” for measuring reactivity and 17 of them met the criteria for being “good”. In addition, the arrival time of the neutron pulse was predicted with a 1σ error of 29 ns with a maximum deviation of 60 ns, providing confidence that a DPF machine is capable of providing a neutron pulse with timing precise enough for use on a dynamic subcritical experiment.

There were 44 shots using DT fuel on SNM Object #2 of which at least 8 neutrons pulses will meet the “good” criteria. The full assessment of the neutron pulse viability using MCNP simulations is not yet complete and therefore the number of “adequate” pulses is currently unknown.

Table 3: Shot summary from Object #1 and #2 testing is divided into shots taken with Tube 1C and Tube 1D.

	Yield ($\times 10^{12}$)	Pulse Shape Characteristics		
		FWHM (ns)	FWTM (ns)	Fall Time (ns)
Object #1	1.53	81.39	174.25	67.07
Object #2: Tube 1C	1.74	90.08	188.44	83.45
Object #2: Tube 1D	0.61	76.39	190.25	95.66

It should be noted, that Object #2 measurements were interrupted by a failure in the Pyrex® insulator between the anode and cathode in Tube 1C. This caused a leak in the vacuum envelope of the tube. Therefore, Tube 1C had to be removed and a new tube (Tube 1D) installed on the DPF mid-campaign. The repair was accomplished in just 3 days, but the incident also unfortunately allowed gaseous contaminants to reach the uranium getter and thereby contaminate the DT gas supply. Once DPF operation resumed the neutron yield was inhibited by the presence of these contaminants even though the tube and the bank were performing as expected. It is anticipated that a new uranium getter with fresh tritium gas will restore DPF performance to the level prior to the tube replacement. A summary of the DT DPF yield and pulse shape metrics obtained during Object #1 and #2 testing is shown in in Table 1.

Area 11 Experiment Setup: Gamma Ray Detector

There are a number of attractive alternatives for the fission gamma ray detector design that vary somewhat in cost and maturity. In order to make good use of the relatively small number of gamma rays that emerge from the system after the neutron flash, the detector system must be both efficient in converting gamma rays to a detectable electronic signal and reasonably large to subtend a sufficient solid angle. The detector must also be designed to measure the fission gamma rays, but not the scattered source or fission neutrons even though they are simultaneously and isotropically being emitted from the SNM object. This is accomplished through time-of-flight separation of the gamma rays and neutrons and the use of shielding to block direct gammas and neutrons produced at the DPF. The length of the flight path required to provide adequate time-of-flight separation between the NDSE gamma signal and the highest energy ($\sim 15\text{MeV}$) neutrons that follow is 15m. There is a direct trade-off between neutron source strength and detector array size. Our studies indicate that, under the assumption of 10^{12} neutrons from the DPF, a 3m X 3 m array of high-efficiency gamma ray detectors constitutes a very conservative approach.

To meet the NDSE detector requirements a sequence of measurements and decision gates were followed: (1) measure the total light output for candidate phototube/scintillation media combinations using gamma rays of various energies; (2) characterize the time response and noise figures for phototubes and photodiodes

using a short pulse laser; (3) measure delayed output components (afterglow) of candidate scintillator/Čerenkov media; (4) evaluate cost versus performance tradeoffs for photomultipliers versus photodiodes and scintillators versus Čerenkov media; and (5) build prototypes and test *in situ* with the DPF. Additional consideration was given to Poisson statistics, including: digitizer bit noise; energy deposition spectrum from the scintillator; decay time and phosphorescence of the scintillator; light collection efficiency (photo-electron statistics); linearity and noise of the PMT, amplifier, and photodiode; after-pulses from the PMT; and the electromagnetic interference (EMI) noise pickup.

NDSE measurements are performed in what are known as “current-mode” as opposed to the single particle “counting-mode” detection techniques used in the DAF. Current mode detection is when many particles (gamma rays in this case) are detected at once with no ability to discriminate between them. The prototype NDSE detector uses a liquid scintillation medium developed by EG&G / Santa Barbara and manufactured by Eljen Technologies of Sweetwater, TX. The decay time for this ultrafast scintillator known as “Liquid VI” is 1.06 ns and is well-matched to NDSE requirements (see Fig. 14). For the SNM static measurements, a 2x2 array of Liquid VI scintillator cells were coupled to 5-inch photomultiplier tubes (PMTs) through a PMMA light-pipe configuration (see Fig. 14). The NDSE Test Stand detector array is significantly smaller ($\sim 0.7\text{m} \times 0.7\text{m}$) than ultimately planned for use in a dynamic subcritical experiment ($\sim 3\text{m} \times 3\text{m}$). It is suitable for measurements of static objects because multiple measurements ($\sim 16\text{--}18$) can be summed together to approximate the signal-to-noise levels that would be obtained for a larger array using only a single DPF pulse.

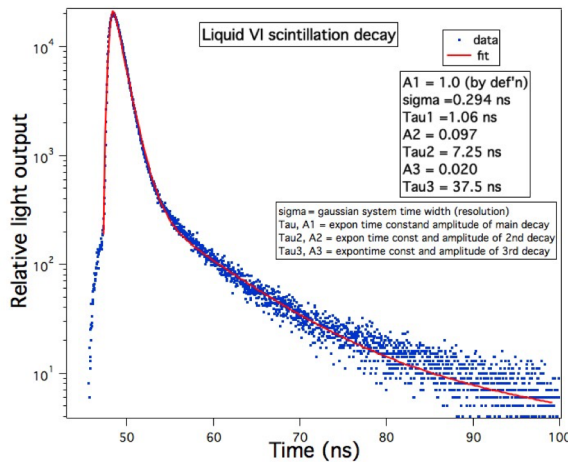


Figure 14: The measured time response for Liquid VI (shown at left) has a 1.06 ns time constant. Four detector modules (shown at right) arranged in a 2x2 array were used for Object #1 and #2 testing at the Area 11 Test Stand.

Although the temporal response of the Liquid VI scintillation media is $\sim 1.06\text{ns}$, the total prototype detector temporal response has been measured to be $\sim 18\text{ns}$. The principal reason for the difference is the large physical size of the scintillator volume

coupled with a dispersive reflective coating applied to the inside walls of the housing. In this environment, the light propagation time associated with multiple reflections for a significant fraction of photons reduces the effective detector bandwidth and this adversely impacts NDSE measurements. Through modeling and simulation of the light transport from the scintillator into the PMT, a new cylindrical detector design has been developed that will improve the temporal response while maintaining γ -ray detection efficiency. The option of implementing smaller photomultiplier tubes is also being investigated as a way to improve detector linearity and further improve bandwidth. These modifications should result in higher signal-to-noise ratios for the detectors and thereby lower uncertainties in the reactivity measurements.

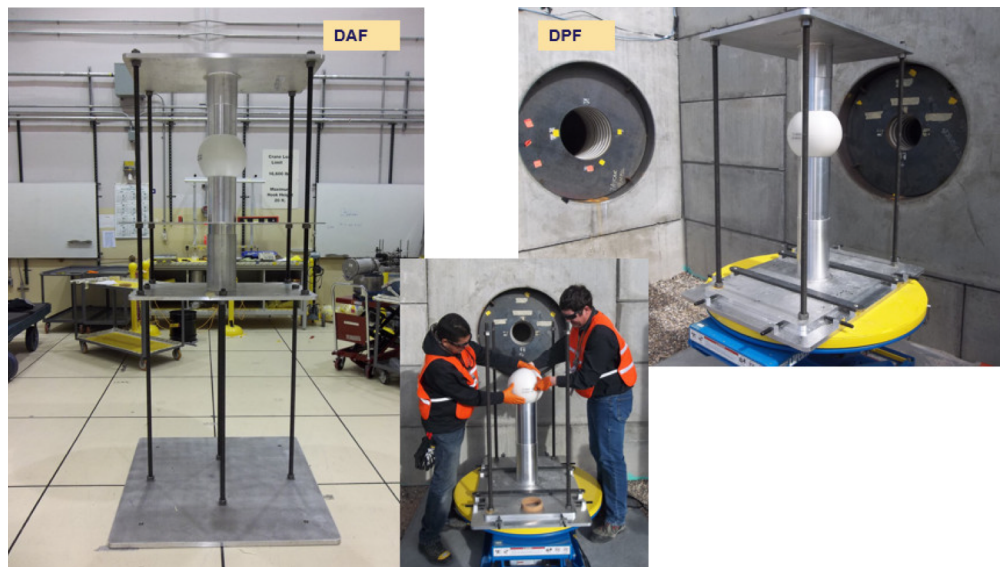


Figure 15. Photographs of the Object 1 in stand at the DAF (left) and at the Area 11 Test Stand placed at the intersection of the DPF LOS (to the right of the stand in photograph on the right) and the gamma detector LOS (to the left of the target).

Object #1 Data and Analysis

NDSE static measurements of SNM Object #1 were conducted during a two-week period in February, 2017. Each day the static object was mounted into the same stand that was used for the DAF measurements. Once mounted into the stand, the object was aligned at the intersection between the collimated neutron line-of-sight from the DPF and the collimated detector line-of-sight. (See Fig. 15) Object #1 was then returned to the DAF for secure overnight storage at the end of each testing day.

The NDSE static results for Object #1 are shown in Fig. 16. Sixteen independent gamma ray detector (blue) and near-in neutron detector (black) measurements are plotted to approximate what a single measurement with a full-size detector wall

would produce. To compare directly with MCNP6 simulations (red) of Object #1, the summed near-in detector measurement (black) is convolved with the gamma ray simulation produced using a delta-function neutron source. Good agreement is obtained between the simulation and measured gamma ray data for the fission fall-off region (6100-6170 ns) which occurs after the neutron peak has gone to zero. Agreement between simulation and data is not good during and near the peak signal (at ~6050 ns) with the data signal being ~30% higher than the calculation. The source of this discrepancy is not currently understood. Several hypotheses exist to explain the difference, including: nuclear cross-section inaccuracies, inelastic scattering neutron scattering processes, and inaccurate time-dependent neutron arrival at the HEU object. These possibilities are all currently under study, however, the degree of correspondence between simulation and measurement after the neutron pulse terminates (the “sweet spot”) is very encouraging confirmation that a dynamic NDSE measurement is feasible.

Two different bounding-case analysis approaches were taken to infer the properties of Object #1 from the static NDSE data. The first assumed no information exists about the shape of the incident DT neutron pulse at the object and instead models it as a delta-function spike. A high-fidelity MCNP6 model of the Area 11 Test Stand was then used to calculate the expected γ -ray fission decay curve shown for Object #1 as measured with the detector array and shown in Figure 17. A fit to this calculation was then varied to show estimates for other k_{eff} values assuming a simple $(1-k_{\text{eff}})$ time scaling. This approach generates a family of possible solutions that can be compared directly with the measured decay curve only in the “sweet spot” after the neutron pulse has ended and before the elastically scattered 14MeV neutrons reach the detector wall. The best match of the simulation folded with a Liquid VI exponential time response function in the region between 6100 and 6150 ns provides a $k_{\text{eff}}=0.942$ and is within ~0.8% of the actual $k_{\text{eff}}=0.9501\pm0.006$. Therefore, with a worst-case assumption about the incident neutron pulse and limiting the comparisons to the “sweet spot” region indicates the k_{eff} can be inferred to ~1%.

The second bounding-case analysis utilizes optimistic assumptions about improving the match between simulation and data during the peak of the neutron pulse. As noted above, current simulations underestimate the size of this peak by approximately 30%. However, if neutron pulse used in the simulations is scaled and the leading-edge shape inferred by arrival of the elastically scattered neutrons at the gamma ray detector wall, then MCNP comparisons with the measured fission decay curve data significantly improve as shown in Figure 18. In this “best case” analysis, the inferred $k_{\text{eff}}=0.947$ and is within ~0.2% of the actual value.

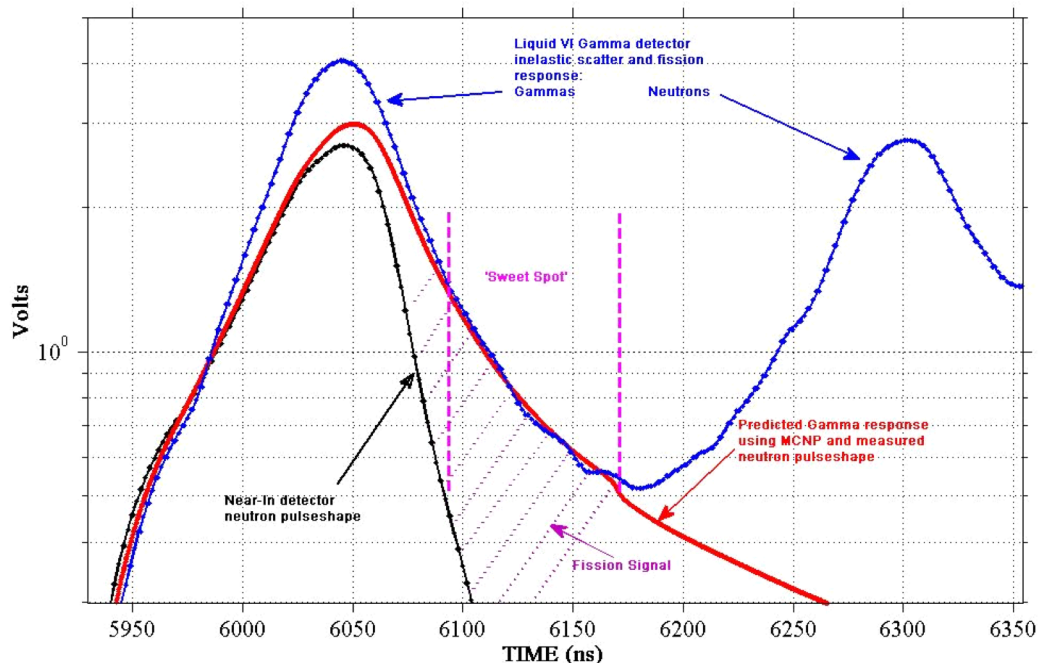


Figure 16. Two weeks of shooting at Area 11 with Object 1 yielded 16 ‘good’ pulses by which it is easiest to see the comparison between data (blue) and MCNP6 calculation (red). There is excellent agreement in the ‘sweet spot’ from 6100-6170 ns, occurring after the DPF source neutrons have ended (black). However, the fit between data and calculation do not agree over the peak at ~6050 ns; this is under investigation. (Time in this plot represents the time after the DPF current switch is turned on.)

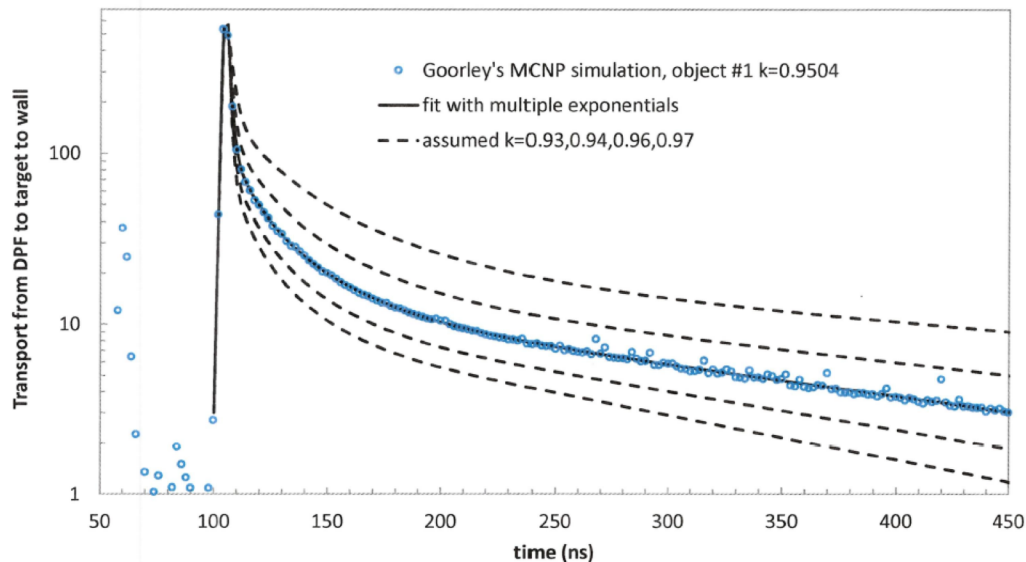


Figure 17. The high-fidelity MCNP6 decay curve simulation Object #1 is shown in blue and a multiple exponential fit to these simulated data is shown with the solid black line. The dashed lines show a $(1-k_{\text{eff}})$ time scaling of this fit to produce a family of possible Object #1 solutions.

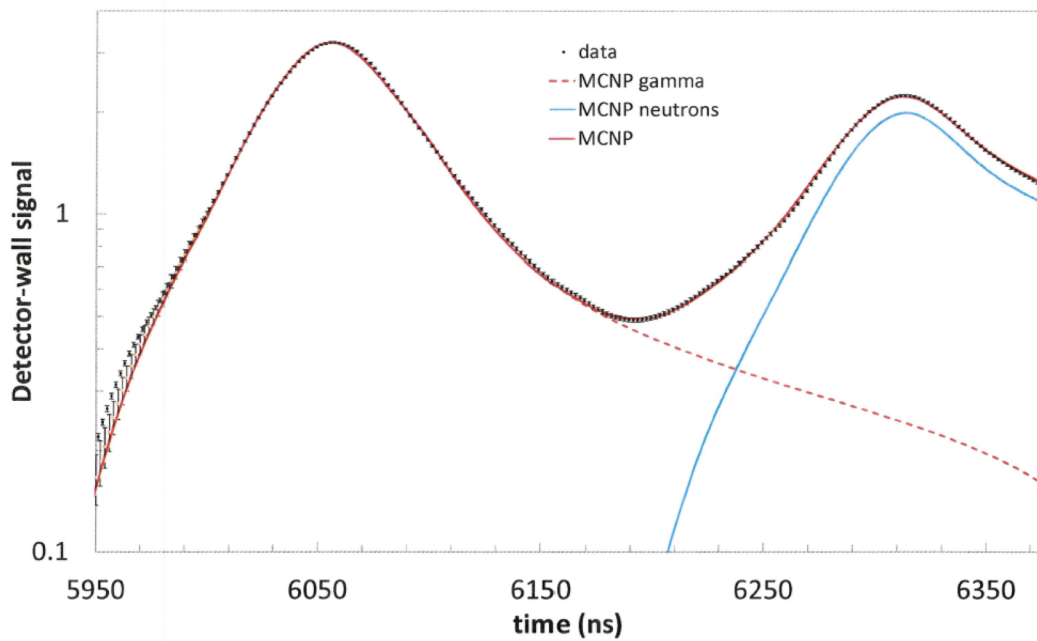


Figure 18. MCNP simulation of the Object #1 NDSE data where the incident neutron pulse was scaled such that the simulation and data match through the peak. This “best case” analysis yields an inferred $k_{\text{eff}}=0.947$ for Object #1 where the family of possible solutions is matched during the peak as well as in the “sweet spot” after the neutron pulse has terminated.

Object #2 Data and Analysis

NDSE static measurements of SNM Object #2 were conducted during a 3-week period in August 2017. Object #2 always remained inside the ICC during transport and measurements at the Area 11 Test Stand due to the aforementioned criticality safety considerations. The Object #1 measured fission decay curves and the Object #2 DAF data provided additional confidence in the Object #2 MCNP simulations. Since the predicted fission decay curve for Object #2 was more intense and less steep after the neutron pulse (See Fig. 19), the Liquid VI detector array was moved to a distance of 20m from the static object thereby providing an additional $\sim 60\text{ns}$ to distinguish and measure the fission gamma fall-off as separate from the prompt signal. The additional γ -ray flux also allowed the PMT voltage and gain to remain similar to that used for Object #1.

Figure 20 shows the data for 13 DPF neutron pulses that were all aligned at the 50% of the fall-off slope. The fission decay curve data compares favorably with the MCNP6 calculation convolved with the neutron source in the ‘sweet spot’ region denoted by the dotted lines. The gamma signal is followed by the arrival of elastically scattered 14MeV neutrons at $\sim 6100\text{ ns}$. It is also interesting to note that Object #2 data shows a distinctive 14 MeV DT neutron peak at $\sim 6200\text{ns}$ followed by a strong fission neutron signal. These fission neutrons create signal in the detector array that is reminiscent of the NUEX data acquired during underground nuclear testing. Bounding case k_{eff} analysis for Object #2 is currently underway.

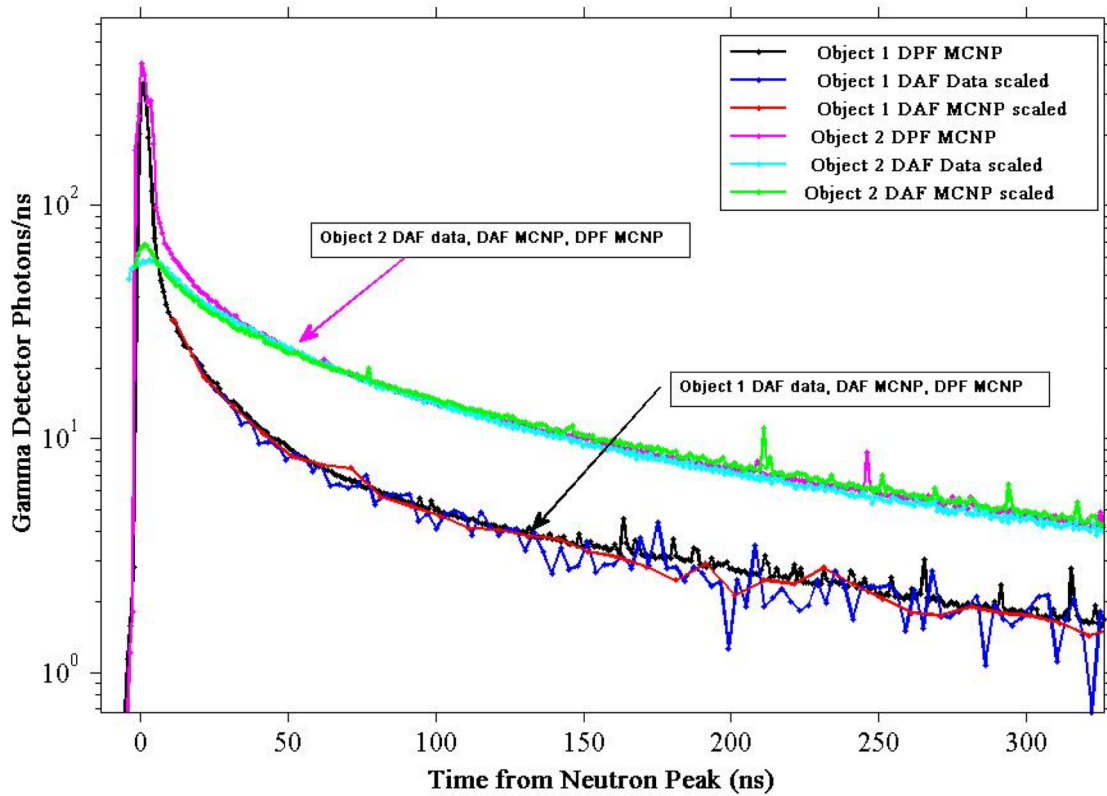


Figure 19. Graphs comparing the Object #1 and #2 data and MCNP6 calculations, included are MCNP6 calculations and predictions for results from Object #1 and #2 using the DPF neutron source.

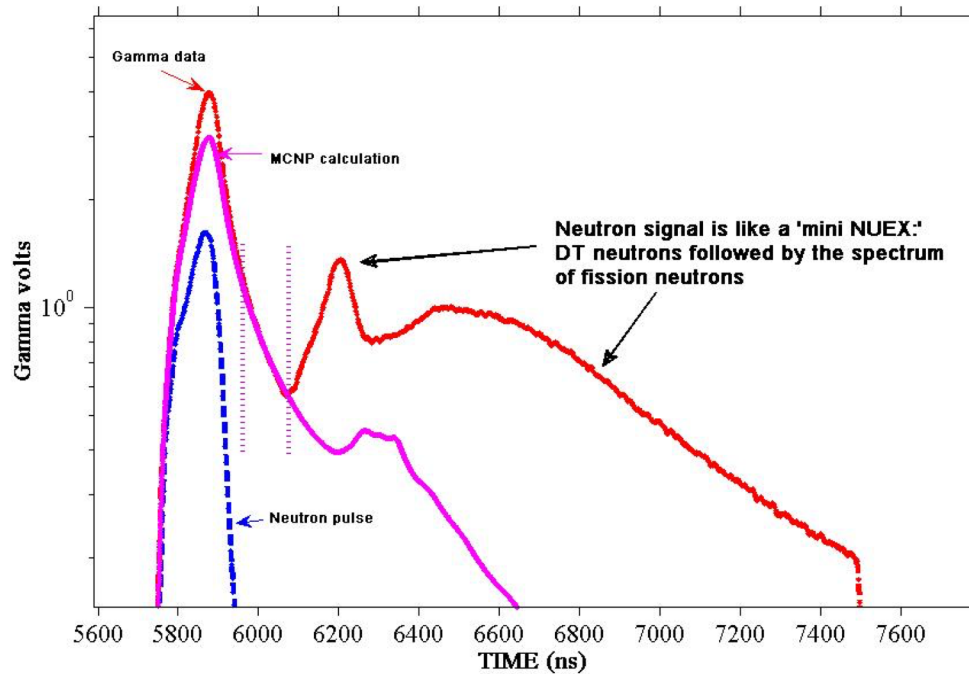


Figure 20. NDSE static data acquired from Object #2 compares favorably with the MCNP6 calculation convolved with the neutron source in the “sweet spot” denoted by the dotted lines. However, just like for Object #1, the MCNP simulation still under predicts the height of the gamma ray signal during the neutron pulse.

Conclusion:

Recall, the principal intent behind the initial set of NDSE measurements using SNM static objects was to demonstrate sensitivity of the technique to fissile systems with different neutronic properties. This goal was successfully met (see Fig. 21) using the DPF-based neutron source, Liquid VI detector array, and the Area 11 Test compound. As expected with any new measurement capability under development, many refinements and improvements to the NDSE technique using a DPF neutron source remain to be addressed before it is implemented on a dynamic subcritical experiment. Some of the main issues are: 1) demonstrating DPF reliability for use on a dynamic experiment; 2) resolving the discrepancy between simulation and data during the DPF pulse; 3) improving the time response of the time-of-flight detector array; 4) quantifying the ability to measure small changes in the neutronic properties of high- k_{eff} SNM objects; and 5) addressing pulsed power and tritium handling safety issues associated with operating a DT DPF in the U1a facility environment.

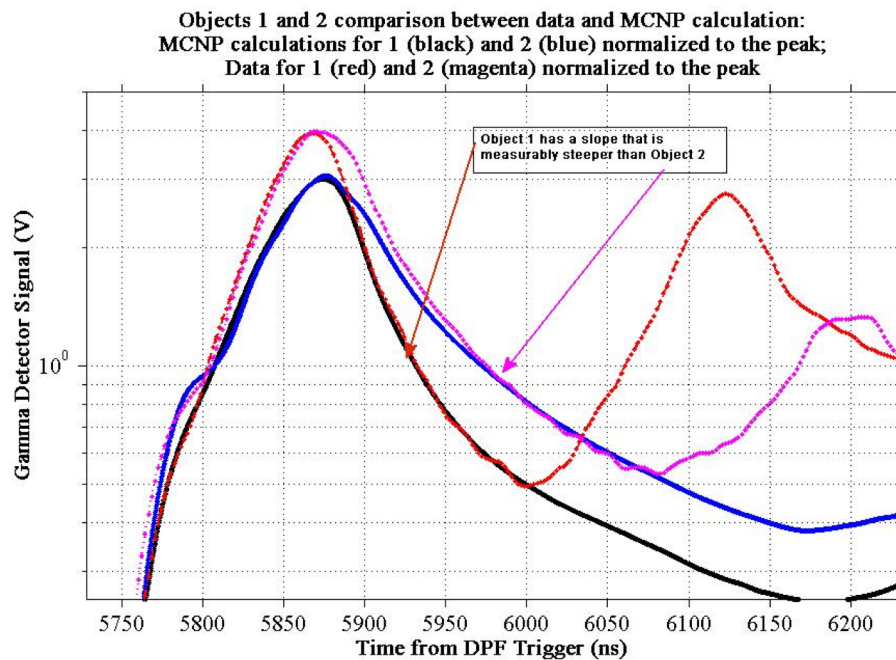


Figure 21. Graphs comparing the Object #1 and #2 data and MCNP6 calculations; Object #2 data and MCNP6 result have been normalized at the peak to those for Object #1. The Object #2 gamma decay curve is distinctly different from that of Object #1, agreeing with MCNP6 calculations; the prompt peak for the data is ~30% larger than MCNP6 calculations for both Objects #1 and #2.

Acknowledgements and Support:

NNSS Nuclear Operations, Device Assembly Facility
NNSS Infrastructure Management and Modernization
NNSS Operations and Infrastructure
NNSS Radiological Control
Centerra Nevada
NA-113 Primary Assessment Technologies
NA-113 Advanced Certification
NA-113 Dynamic Material Properties
NA-113 Advanced Radiography
NA-50
NA-70